



# City Research Online

## City St George's, University of London

**Citation:** Mozafari, M., Sadeghimalekabadi, M., Fardi, A., Bruecker, C. & Masdari, M. (2024). Aeroacoustic investigation of a ducted wind turbine employing bio-inspired airfoil profiles. *Physics of Fluids*, 36(4), 041918. doi: 10.1063/5.0204050

This is the accepted version of the paper.

This version of the publication may differ from the final published version. To cite this item please consult the publisher's version.

**Permanent repository link:** <https://openaccess.city.ac.uk/id/eprint/32898/>

**Link to published version:** <https://doi.org/10.1063/5.0204050>

**Copyright and Reuse:** Copyright and Moral Rights remain with the author(s) and/or copyright holders. Copies of full items can be used for personal research or study, educational, or not-for-profit purposes without prior permission or charge, unless otherwise indicated, provided that the authors, title and full bibliographic details are credited, a hyperlink and/or URL is given for the original metadata page and the content is not changed in any way. For full details of reuse please refer to [City Research Online policy](#).

This is the author's peer reviewed, accepted manuscript. However, the online version of record will be different from this version once it has been copyedited and typeset.

PLEASE CITE THIS ARTICLE AS DOI: 10.1063/1.50204050

1 **Aeroacoustic investigation of a ducted wind turbine employing bio-**  
 2 **inspired airfoil profiles**

3 Mostafa Mozafari,<sup>1</sup> Mahyar Sadeghi Malekabadi,<sup>2</sup> Amirhosein Fardi<sup>3</sup>, Christoph Bruecker<sup>4</sup>  
 4 and Mehran Masdari<sup>5</sup>.

5 <sup>1</sup> Faculty of New Sciences and Technologies, University of Tehran, Tehran, Iran.

6 <sup>2</sup> Faculty of Aerospace Engineering, Sharif University of Technology, Tehran, Iran.

7 <sup>3</sup> Faculty of Mechanical Engineering, Lakehead University, Thunder Bay, ON P7B 5E1, Canada.

8 <sup>4,5</sup> City, University of London, Northampton Square, London, EC1V 0HB, UK.

9 Correspondence should be addressed to Mehran Masdari; [mehran.masdari@city.ac.uk](mailto:mehran.masdari@city.ac.uk)

10

11 **Abstract**

12 Ducted wind turbines for residential purposes are characterized by a lower diameter with  
 13 respect to conventional wind turbines for on-shore applications. The noise generated by the  
 14 rotor plays a significant role in the overall aerodynamic noise. By making modifications to the  
 15 blade sections of the wind turbine, we can alter the contributions of aeroacoustic noise sources.  
 16 This study introduces innovative wind turbine blade designs inspired by owl wing  
 17 characteristics, achieving significant noise reduction without compromising aerodynamic  
 18 performance. A three-dimensional (3D) scan of an owl wing was first employed to derive a  
 19 family of airfoils. The airfoils were employed to modify the blade of a referenced wind turbine  
 20 airfoil section at various positions on the blade span to determine a blade operating more  
 21 efficiently at the tip-speed ratio of the original one. While maintaining the same aerodynamic  
 22 performance, the bio-inspired profiles show a more uniform pressure coefficient distribution,  
 23 considerably decreasing in the noise level. Furthermore, this study makes considerable  
 24 progress in ducted wind turbine design by obtaining an 8 dB noise reduction and a 12%  
 25 improvement in sound pressure level. An in-depth aerodynamic examination shows a 6.4% rise  
 26 in thrust force coefficient and optimized power coefficients, reaching a peak at a Tip Speed  
 27 Ratio (TSR) of 8, demonstrating improved energy conversion efficiency. The results highlight  
 28 the dual advantage of the innovative design: significant noise reduction and enhanced  
 29 aerodynamic efficiency, offering a promising alternative for urban wind generation.  
 30

31 **Keywords:** Ducted Wind Turbine, Aeroacoustics, Barn Owl, Large Eddy Simulation.

32 **Nomenclatures**

AOA	Angle of Attack	$C_T$	thrust force coefficient
$c$	Chord of Airfoil	TSR	Tip Speed Ratio
$C_l$	Lift Coefficient	SPL	Sound Pressure Level
$C_d$	Drag Coefficient	OASPL	Overall Sound Pressure Level
$C_l/C_d$	Lift-to-drag ratio	$C_{PWR}$	Power Coefficient
2D / 3D	Two / Three Dimensional	LES	Large Eddy Simulation
WT	Wind Turbine	FW-H	Ffowcs Williams-Hawkings
DWT	Ducted Wind Turbine	CFD	Computational Fluid Dynamics

### 33 Introduction

34 The effect of rising global warming has shifted the world to clean energy sources; the most  
 35 efficient source of clean energy is wind energy [1]. The use of such renewable energy has  
 36 grown rapidly [2], to the point of justifying the usage of wind turbines in profitable locations  
 37 in urban areas, to reduce the costs of energy delivery to the user. The integration in the urban  
 38 environment comes at the cost of reducing the rotor sizes of the wind turbine, by adding a duct  
 39 to increase the incoming flow speed lowering the effect of incoming turbulent fluctuations, and  
 40 having to respect more stringent aeroacoustic regulations [3].

41 The reduction of the wind turbine rotor changes the contributions of the aeroacoustic noise  
 42 sources, since the turbine is now operating at a relatively lower Reynolds number and at a much  
 43 higher rotational speed than a conventional one. In this respect, the loading and thickness  
 44 contributions are no longer negligible. The overall aerodynamic noise is a combination of the  
 45 one produced by the rotor and the one determined by the duct. While a lot of studies have  
 46 focused on the coupling between the duct or diffuser and the rotor, only a few have proposed  
 47 the use of specific airfoils for such low Reynolds number and high turbulence applications.  
 48 Bio-inspired airfoils have been shown to possess particular characteristics to allow birds to fly  
 49 in very turbulent environments, with an extremely high lift-to-drag ratio, and at the same time  
 50 do silently [4]. This has inspired the use of such airfoils for drones and small rotor applications.  
 51 Despite being known for their feather characteristics, owl's wings have an additional  
 52 characteristic. The high lift-to-drag ratio of the profile, allows the bird to enormously reduce  
 53 the flying speed to sustain the bird's weight. Combined with the additional serrated leading  
 54 edge, the velvety surface and the fringes at the trailing edge, the owl's wing performance is the  
 55 most silent in the animal kingdom in the final phase of attacking the prey [5-7]. From an  
 56 aerodynamic point of view the combination of the previous factors, seems to also produce a  
 57 more favorable and thinner boundary layer, which helps in increasing the aerodynamic  
 58 performance of the wing. Various studies have been performed experimentally [8, 9],  
 59 numerically [10-12] and in real flight [13] to use the owl wing characteristics.

60 In the realm of aerodynamics, flow and noise control are pivotal for enhancing the performance  
 61 and reducing the environmental impact of wind turbines. Two primary methods are employed  
 62 to achieve these objectives: active and passive flow control techniques. Active methods, such  
 63 as the use of dielectric barrier discharge plasma actuators demonstrated by Lee et al. [14],  
 64 actively manipulate the flow field around structures to control separation and reduce drag,  
 65 thereby influencing noise generation. On the other hand, passive methods involve structural  
 66 modifications to the body, which passively influence the flow and noise characteristics. An  
 67 example is the use of grooved surfaces on deflectors to improve the aerodynamic performance  
 68 of Savonius wind turbines, as explored by Fatahian et al. [15]. This research aligns with passive  
 69 flow control strategies by adopting a bio-inspired model that leverages the silent flight  
 70 characteristics of owl wings. The integration of airfoil profiles inspired by the natural wing  
 71 structure of owls represents a novel approach in the design of ducted wind turbines to passively  
 72 control flow and reduce noise. Such bio-inspired designs, as evidenced by the comparative  
 73 analysis of flow control over a circular cylinder with detached flexible and rigid splitter plates  
 74 by Eydi et al. [16], underscore the potential of nature-inspired solutions in engineering  
 75 applications. Our study builds upon this foundation, employing passive flow control through  
 76 bio-mimicry to achieve a harmonious balance between aerodynamic efficiency and noise  
 77 reduction in wind turbine design. Additionally, Song et al. [17] demonstrated that the bionic  
 78 edge design strategy can effectively control the turbulent flow field and effectively break down  
 79 airflow near the trailing edge. This leads to improved thrust and decreased noise levels.

This is the author's peer reviewed, accepted manuscript. However, the online version of record will be different from this version once it has been copyedited and typeset.

PLEASE CITE THIS ARTICLE AS DOI: 10.1063/1.5204050

80 According to the literature review in this study, it was concluded that very few studies focused  
 81 on isolating the airfoil characteristics and employing them for industrial applications. In a study  
 82 by Liu et al. [18], a laser scanner was used to scan the owl wing and characterize its geometric  
 83 characteristics. These characteristics included camber, chord, twist, and thickness distribution.  
 84 An analysis of flow interactions with surfaces and flow physics surrounding an owl airfoil was  
 85 conducted by Klan et al. [19]. Bachmann et al. [20] provided a comprehensive characterization  
 86 of the wings and feathers of barn owls in high spatial resolution. They conclude that barn owls  
 87 have evolved specialized wings and feathers to reduce flight noise. To investigate the wings at  
 88 high spatial resolution, they used confocal laser scanning microscopy, surface digitizing, and  
 89 computed tomography. They found that these birds of prey have huge wings relative to their  
 90 body mass, which enables slow flights with increased maneuverability. At low speeds, the  
 91 researchers found that modifications to the wings' surfaces and edges helped stabilize airflow.  
 92 Geyer et al. [21] conducted a comprehensive study on owl wings. In addition to performing  
 93 numerical calculations, they conducted laboratory tests on the wings of owls and several other  
 94 birds. According to their findings, an owl's wings can be 20 decibels quieter than other birds'  
 95 wings when gliding. This was achieved by exploiting the relatively lower speed at which the  
 96 owl's profile was able to operate. Kondo et al. [22] studied the aerodynamic characteristics of  
 97 an owl-like airfoil at a Reynolds number of 2300. Their results indicate that the deeply concave  
 98 lower surface of the owl-like airfoil contributes to lift augmentation, and both a round leading  
 99 edge and a flat upper surface lead to lift enhancement and drag reduction, determined by the  
 100 presence of a thin laminar separation bubble near the leading edge. Subsequently, the owl-like  
 101 airfoil has a higher lift-to-drag ratio than the high lift-to-drag Ishii airfoil at low Reynolds  
 102 number. A new airfoil for the wind turbine blades was designed and used in the wind turbine  
 103 blades by Tian et al. [23]. Results show that the bio-inspired airfoil inspired by the Long-eared  
 104 Owl's wing has a superior lift coefficient and stalling performance, and thus can enhance wind  
 105 turbine blade performance. An owl inspired airfoil without serrations and a Downy wing  
 106 surface was compared to a NACA airfoil at low Reynolds numbers by Anyoji et al. [24].  
 107 According to their results, the owl inspired airfoil has more lift and generally performs better  
 108 than the base airfoil at low Reynolds numbers. Moslem et al. [25] demonstrated that a  
 109 bioinspired propeller not only diminishes both harmonic and broadband noise but also achieves  
 110 a superior noise level compared to the baseline configuration. Aono et al. [26] investigated the  
 111 aerodynamics of an owl wing-like airfoil for low Reynolds numbers using numerical methods  
 112 and the LES turbulence model. They compared the simulation results with several conventional  
 113 airfoils and showed that the owl wing-inspired airfoil has a higher lift-to-drag coefficient than  
 114 the other airfoils compared. They reported that this increase was due to the creation of a high-  
 115 pressure area in the suction area of the airfoil due to the curvature of the owl airfoil.  
 116 Muthuramalingam et al. [27] explored laminar flow control by employing leading-edge  
 117 serration, demonstrating a postponement in the transition from laminar to turbulent flow. This  
 118 effect parallels the phenomenon observed in owl flight, contributing to further noise reduction.  
 119 Despite all the previous results, whether these airfoils can be reliably applied for a rotating  
 120 blade at low Reynolds number is still under debate. While in fact the aspect ratio is very similar,  
 121 the loading distribution of a rotating blade is relatively different from the distribution of a bird's  
 122 wing in gliding conditions.

123 In this manuscript, an investigation is made to study how bio-inspired airfoils could be  
 124 employed to outperform the loading distribution of a rotating blade. The study proceeds by  
 125 evaluating how the aerodynamic performance would affect the aeroacoustic footprint of the  
 126 rotor, including loading and thickness noise and discussing the broadband part due to the  
 127 change in boundary layer characteristics. The manuscript is organized as follows: In section 2  
 128 of this research, a family of airfoils is produced through 3D scanning. These airfoils are then

This is the author's peer reviewed, accepted manuscript. However, the online version of record will be different from this version once it has been copyedited and typeset.

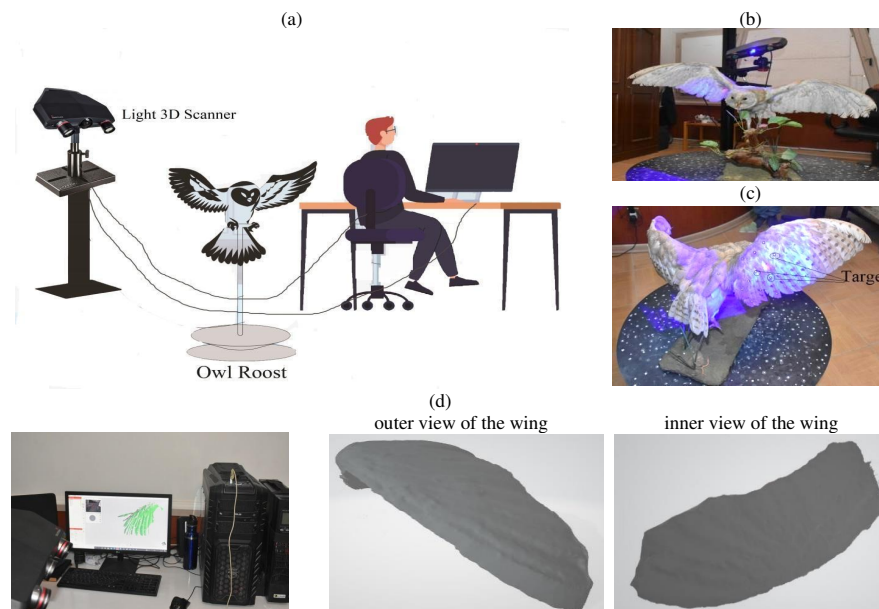
PLEASE CITE THIS ARTICLE AS DOI: 10.1063/1.5204050

129 utilized in the design of ducted wind turbine blades, as detailed in section 3. The following  
 130 sections present a comprehensive numerical analysis of cases (benchmark and multi-section  
 131 blades), along with the results of aerodynamic and aeroacoustic prediction.

132 **Airfoil family generation**

133 To generate a family of bio-inspired airfoils, a taxidermy owl as shown in Figure 1 has been  
 134 placed in the center of a 3D scanner. Circular targets mark the owl wing to allow for combining  
 135 multiple fields of view in a unique 3D reconstruction. In this test, the Solutionix  
 136 C500-Structured Light 3D Scanner has been used, with a final reconstruction accuracy of 0.01  
 137 mm. The center points of the wing are relatively less accurate, due to possible errors induced  
 138 by the presence of the velvet surface and the feathers.

139 Illustrated below is the barn owl wing alongside its corresponding reverse model (Figure 2).  
 140 The airfoil sections exhibit varying airfoil shapes and chord lengths. The data fitting procedure  
 141 involved using MATLAB to employ Polynomial fitting. For both the upper and lower surfaces  
 142 of the airfoil, an independent polynomial of degree six was selected. Figure 3 provides an  
 143 illustrative instance featuring the root airfoil, offering a visualization of its equations and the  
 144 associated fitting curve.



145 Figure 1: the experimental set-up. (a) A general illustration of the experimental setup. (b) An owl with the  
 146 camera laser (c) A close view of the laser light sheet with targets on the owl wing (d) 3-D scan output of the  
 147 owl's wing.

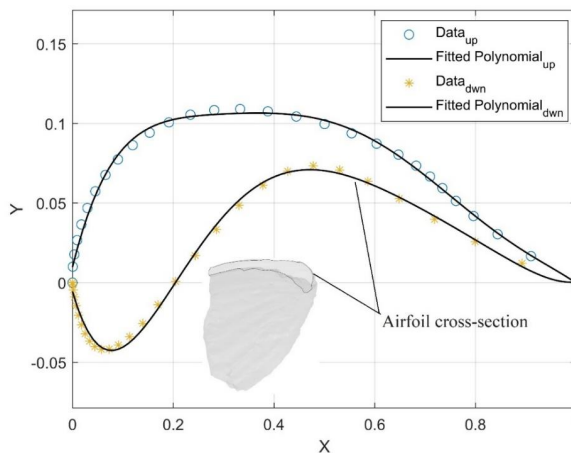
This is the author's peer reviewed, accepted manuscript. However, the online version of record will be different from this version once it has been copyedited and typeset.

PLEASE CITE THIS ARTICLE AS DOI: 10.1063/1.5204050



148

Figure 2: (a) Barn owl wing, (b) inverted owl wing model.



149

150

Figure 3: Fitting Results for Airfoil Profile.

151 The extracted airfoil exhibits a maximum thickness of 12% at  $x/c=0.11$ . In the study by Klan  
 152 et al. [19], these characteristics are documented as 14.77% and 0.15, respectively. It's important  
 153 to acknowledge a slight variance in the airfoil's overall specifications, potentially stemming  
 154 from the owl's taxidermy process and water loss from the bird's body. Furthermore, the airfoil  
 155 features a cusp-type trailing edge, consistent with the research of Ricks et al. [28], which  
 156 suggests that such a slender trailing edge is associated with reduced noise generation. As  
 157 indicated, the spatial arrangement of the upper and lower airfoil surfaces has been  
 158 approximated using a 6<sup>th</sup> degree polynomial function. This function, denoted as  
 159  $y_c = ax^6 + bx^5 + cx^4 + dx^3 + ex^2 + fx + g$ , has coefficients detailed in Table 1. Here, 'x' represents  
 160 the positional coordinates along the direction of the airfoil chord.

161

Table 1: Polynomial Coefficients for Geometric Approximation of Airfoil Surfaces.

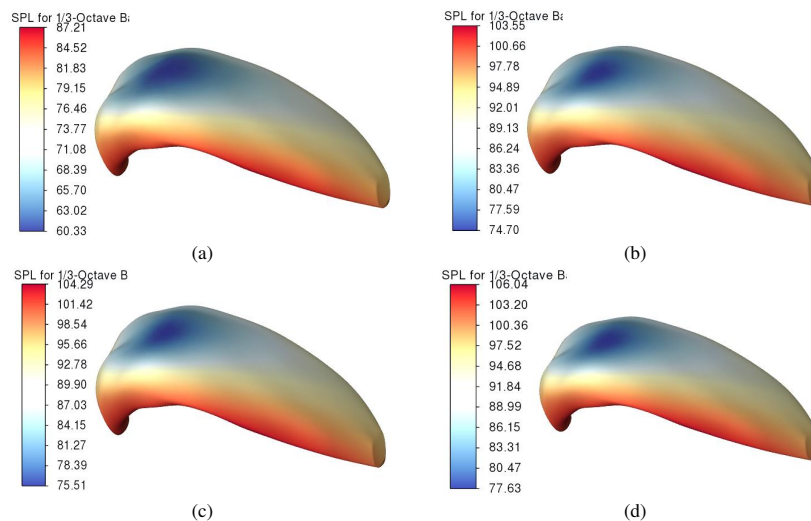
Type	a	b	c	d	e	f	g
upper surface	-6.62	23	-30.77	20.1	-6.98	1.266	0.01
lower surface	7.76	-28.33	41.31	-29.72	10.10	-1.1	-0.0056

This is the author's peer reviewed, accepted manuscript. However, the online version of record will be different from this version once it has been copyedited and typeset.

PLEASE CITE THIS ARTICLE AS DOI: 10.1063/1.5204050

162 **Blade Design**

163 After scanning the owl's wing, as depicted in Figure 4, a comprehensive numerical analysis  
 164 was conducted in the vicinity of the owl's wing across a range of frequencies. The simulation  
 165 was carried out using ANSYS-FLUENT software, employing the LES turbulence model and  
 166 FW-H acoustic analogy. The domain is subjected to boundary conditions, with velocity inlet  
 167 and pressure outlet. Additionally, a symmetry condition is applied to surface included the wing  
 168 root. The computational domain had dimensions of 0.5 \* 0.8 \* 2 meters, with a mesh count of  
 169 0.5 million. Based on sound pressure level measurements conducted by Gruschka et al. [29], it  
 170 was established that the owl's sound remains inaudible beyond a 3-meter distance for  
 171 frequencies below 2000 Hz. Consequently, it was decided to incorporate SPL contour tuned to  
 172 frequencies of 500, 1000, 1600, and 2000 Hz. Moreover, a recurring pattern can be observed  
 173 across different frequencies in all four cases. Additionally, the following section presents the  
 174 OASPL curve for the wing sections along the span direction. Upon examination of this curve,  
 175 it became evident that specific locations along the span of the owl's wing consistently exhibited  
 176 lower noise levels compared to others. Consequently, these positions were selected as the  
 177 preferred locations for airfoil extraction. In the selection of these positions, careful  
 178 consideration was given to choose justifiable points within the range. These positions were  
 179 identified at 3%, 12.5%, 27%, 44%, and 68% of the owl wing's span, respectively. The  
 180 reduction in noise during owl flight was attributed to the distinctive characteristics of its airfoil.



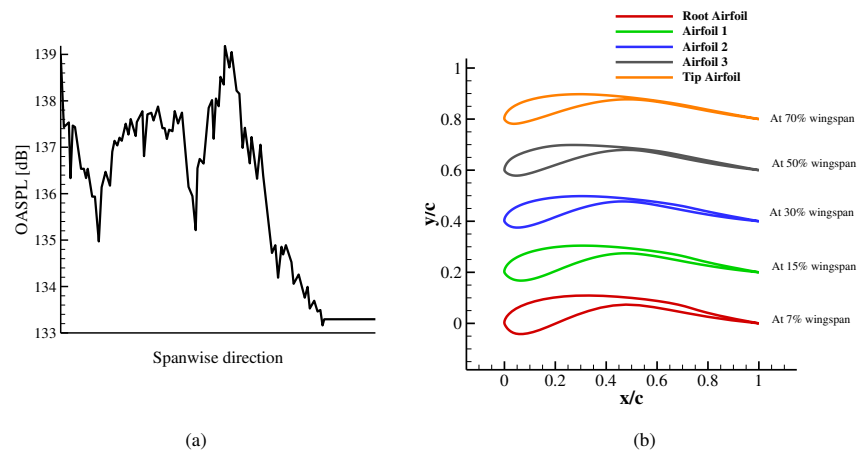
181 Figure 4: Noise level contours (a) 500 Hz, (b) 1 kHz, (c) 1.6 kHz and (d) 2 kHz.

182 In light of this discovery, as depicted in Figure 5a, the decision was made to extract and employ  
 183 these airfoil characteristics from the owl's wing as the preferred airfoil profiles for blade design.  
 184 The distribution of OASPL shows minimal variations along the owl's wingspan. Interpolation  
 185 has been utilized to pinpoint cross-sectional data, with selections made at intervals of 7%, 15%,  
 186 30%, 50%, and 70% of the blade span. To align with the structural characteristics of the WT,

This is the author's peer reviewed, accepted manuscript. However, the online version of record will be different from this version once it has been copyedited and typeset.

PLEASE CITE THIS ARTICLE AS DOI: 10.1063/1.5204050

187 the airfoil for the WT is chosen based on approximately 70% of the actual owl wing (Arm  
 188 wing). The selected positions of the airfoils are approximately consistent with the minimum  
 189 locations in the OASPL curve. Consequently, the airfoil of the last section is selected as the tip  
 190 airfoil for the wind turbine. Wolf and Konrath [30] conducted measurements of the three-  
 191 dimensional shape of an owl's wing during a flapping cycle. The airfoils derived from the wings  
 192 of the taxidermy owl examined in this study closely resemble the configuration observed  
 193 during the gliding phase at a position approximately 5 meters along the right-to-left flight  
 194 direction. Furthermore, as shown in Figure 5b, these acquired airfoil profiles were utilized to  
 195 create various sections of the ducted wind turbine. These airfoils were subsequently  
 196 proportionally scaled and adjusted according to the specifications outlined in Table 2 to align  
 197 with the design requirements of the desired wind turbine. The ducted wind turbine is designed  
 198 based on the owl's wing but with some modifications to improve the noise reduction for urban  
 199 installations.

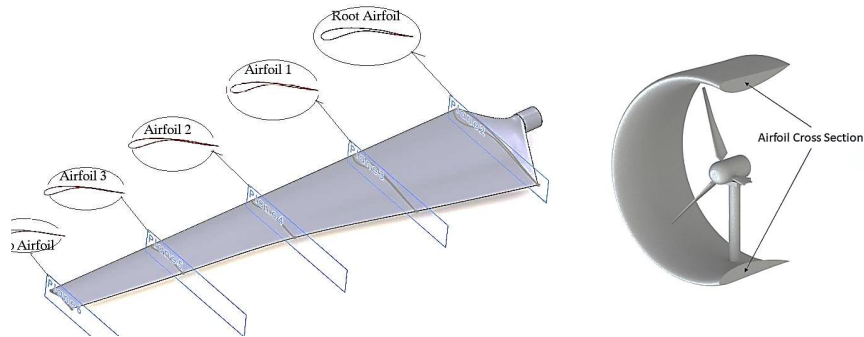


200 Figure 5: (a) the distribution curve of OASPL in the spanwise direction and illustrating the definition of the  
 201 position of the selected airfoils, (b) Airfoils section inspired by owl wings.

202 As depicted in Figure 6, the airfoils for various sections draw inspiration from owl wings in  
 203 shaping the desired geometry (refer to Table 2). Within the framework of DWT blade design,  
 204 a consistent airfoil is established within each of the delineated sections. However, to seamlessly  
 205 interlink these sections, the loft feature is implemented in CAD Software, allowing for  
 206 adaptable variation of the airfoil along the span. The turbine has a duct length of 1 meter and  
 207 an internal diameter of 1.6 meters.

This is the author's peer reviewed, accepted manuscript. However, the online version of record will be different from this version once it has been copyedited and typeset.

PLEASE CITE THIS ARTICLE AS DOI: 10.1063/1.50204050



208 Figure 6: Schematic of the ducted wind turbine and multi-section blade.

209

Table 2: Design Features of Turbine.

Airfoils	Chord (m)
Root Airfoil	0.16
Airfoil 1	0.12
Airfoil 2	0.08
Airfoil 3	0.06
Tip Airfoil	0.04
Duct Airfoil	1

210 **Cases examined**

211 This research involved two simulations, which are described in brief below. In this  
 212 simulation, unsteady, compressible conditions are used in conjunction with LES turbulence  
 213 model and FW-H acoustic analogy.

- 214 1. Case 1: (Benchmark Blade- DonQi® wind turbine [31]).
- 215 2. Case 2: (Multi-section Blade) Use of airfoils of different sections of the owl wing  
 216 for blade sections: This case was done to investigate the effect of changing the  
 217 airfoil and the use of airfoils of different sections of the owl wing in different  
 218 sections of the blade.

219 **Governing equations**

220 This study utilized computational fluid dynamics with the Large Eddy Simulation (LES)  
 221 method for fluid flow analysis and the Ffowcs Williams and Hawkins (FW-H) acoustic  
 222 analogy for acoustic analysis. The governing equations for each method are detailed below.

223 **Fluid dynamics**

224 Turbulent flows are characterized by eddies with a wide range of length and time scales. In the  
 225 Large Eddy Simulation (LES) method, large eddies are solved directly and small eddies are  
 226 also modeled. The governing equations employed for LES are obtained by filtering the time-  
 227 dependent Navier-Stokes equations in either Fourier (wave-number) space or configuration  
 228 (physical) space. Filtering the Navier-Stokes equations, one obtains [32]:

$$\frac{\partial \rho}{\partial t} + \frac{\partial}{\partial x_i} (\rho u_i) = 0 \quad (1)$$

229 And

$$\frac{\partial}{\partial t} (\rho \bar{u}_i) + \frac{\partial}{\partial x_j} (\rho \bar{u}_i \bar{u}_j) = \frac{\partial}{\partial x_j} \left( \mu \frac{\partial \sigma_{ij}}{\partial x_j} \right) - \frac{\partial \bar{p}}{\partial x_i} - \frac{\partial \tau_{ij}}{\partial x_j} \quad (2)$$

230 where  $u$ ,  $\rho$ ,  $\mu$  and  $p$  are the fluid velocity, density, turbulent viscosity, and static pressure,  
 231 and  $i$  and  $j$  are the subscripts with 1 and 2 for the  $x$  and  $y$  directions. Also,  $\sigma_{ij}$  is the stress  
 232 tensor due to molecular viscosity and  $\tau_{ij}$  is the subgrid-scale stress.

233 **Acoustics**

234 Lighthill proposed the theory of the difference between real flow and reference flow and called  
 235 it analogy. Ffowcs Williams-Hawkins (FW-H) then challenged it and used to give solutions  
 236 to Lighthill's equation for a medium that includes moving surfaces and convected turbulent  
 237 flow. In this research, FW-H formulation has been used to model the propagation of sound  
 238 from a moving source [33, 34].

$$\begin{aligned} \frac{1}{c_\infty^2} \frac{\partial^2 p'}{\partial t^2} - \frac{\partial^2 p'}{\partial x_i^2} = \frac{\partial^2}{\partial x_i \partial x_j} \{T_{ij} H(f)\} - \frac{\partial}{\partial x_i} \{[P_{ij} n_j + \rho u_i (u_n - v_n)] \delta(f)\} \\ + \frac{\partial}{\partial t} \{[\rho_\infty v_n + \rho (u_n - v_n)] \delta(f)\} \end{aligned} \quad (3)$$

239 Where  $u_n$  and  $u_i$  are the fluid velocity in the normal direction of the integration surface and  
 240 in  $x_i$  direction, respectively.  $v_n$  and  $v_i$  represent the normal velocity of the integration surface  
 241 and the surface velocity component in  $x_i$  direction.  $H(f)$  is Heaviside function and  $\delta(f)$  is  
 242 Dirac delta function.  $p'$  is sound pressure in the far field ( $p' = p - p_\infty$ ),  $n_j$  normal vector  
 243 pointing to the external area ( $f > 0$ ),  $c_\infty$  is speed of sound in the far field,  $P_{ij}$  is compressive  
 244 stress tensor and  $T_{ij}$  is the Lighthill's stress tensor, given by:

$$T_{ij} = \rho v_i v_j + p_{ij} - (\rho - \rho_\infty) c_\infty^2 \delta_{ij} \quad (4)$$

245 To solve Equation (3), the Green's function must be used to the open area. The complete  
 246 solution involves the calculation of surface and volume integrals, the first representing  
 247 monopole, dipole, and partially quadrupole acoustic sources, and the second representing  
 248 quadrupole sources in the area outside of the source surface. The volume integral becomes  
 249 negligible when the Mach number value of the flow is small and the source area covers the  
 250 source area. In Ansys Fluent, choosing a source on a solid surface-like rotor, the volume  
 251 integrals are neglected, and then the equation takes the following form [35]:

$$p'(\vec{x}, t) = p'_T(\vec{x}, t) + p'_L(\vec{x}, t) \quad (5)$$

252 In equation (5),  $t$  is the observer time,  $\vec{x}$  is the receiver position. The subscripts T and L. L  
 253 refer to the thickness (monopole) and loading (dipole) components, respectively and are given  
 254 as follows [33, 34]:

$$4\pi p'_T(\vec{x}, t) = \int_{f=0} \left[ \frac{\rho_\infty (\dot{U}_n + U_n)}{r(1-M_r)^2} \right] ds + \int_{f=0} \left[ \frac{\rho_\infty U_n (r\dot{M}_r + c_\infty (M_r - M^2))}{r^2(1-M_r)^3} \right] ds \quad (6)$$

$$4\pi p'_L(\vec{x}, t) = \frac{1}{c_\infty} \int_{f=0} \left[ \frac{\dot{L}_r}{r(1-M_r)^2} \right] ds + \int_{f=0} \left[ \frac{L_r - L_M}{r(1-M_r)^2} \right] ds \\ + \frac{1}{c_\infty} \int_{f=0} \left[ \frac{L_r \left\{ r\dot{M}_r + c_\infty (\dot{M}_r - M^2) \right\}}{r^2(1-M_r)^3} \right] ds \quad (17)$$

255 Where:

$$256 \quad U_i = v_i + \frac{\rho}{\rho_\infty} (u_i - v_i) \\ L_i = P_{ij} \hat{n}_j + \rho u_i (u_n - v_n)$$

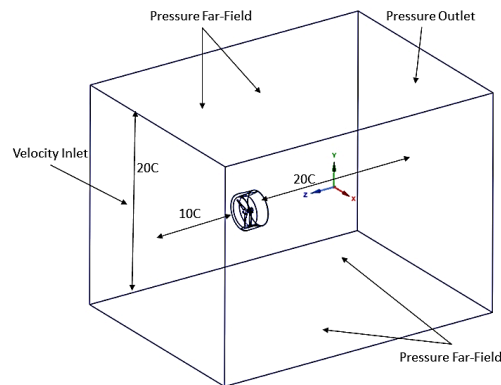
257 Where  $M$  and  $r$  represent the surface velocity vector and the unit radiation vector. The two  
 258 terms  $p'_T(\vec{x}, t)$  and  $p'_L(\vec{x}, t)$  in Equation (5) are referred to as thickness and loading terms,  
 259 respectively.

#### 260 Numerical solver

261 The commercial software ANSYS-FLUENT has been used for all simulations carried out in  
 262 this work. For an accurate calculation of the flow field around the blade, the LES solution was  
 263 calculated with the Fluent SIMPLE solver. This approach has been proven suitable to describe  
 264 similar problems in wind turbines. This solver used the finite volume method as a discretization  
 265 procedure with Bounded Central Differences for momentum and Second Order Central  
 266 Differences for pressure. A Bounded Second Order Implicit scheme is used for the time  
 267 marching method in the present work as a temporal discretization scheme with the convergence  
 268 criteria of  $10^{-4}$ . Since the Mach number at the blades of a wind turbine is always less than 0.2,  
 269 the air has been modeled as incompressible for reducing the computational costs while  
 270 maintaining accuracy.

271 The 3D mesh of the full rotor was carried out first by drawing it in the SpaceClaim software,  
 272 while the mesh generation was performed using Fluent Meshing. For this problem, a  
 273 polyhexcore mesh is generated. The computational domain is divided into two parts: the  
 274 internal rotating field and the external relatively stationary flow field. The interfaces are set to  
 275 transfer data between the rotational and stationary parts. Coupled problems between the two  
 276 parts have a significant influence on the accuracy of numerical simulation. In the present study,  
 277 the sliding mesh model is used to account for the rotation of the blades.

278 Figure 7 shows the boundary conditions, including velocity inlet and pressure outlet boundaries  
 279 used to simulate the far field flow. In this case, the velocity of the free stream is 5 m/s,  
 280 corresponding to the Reynolds number ( $Re$ ) based on the duct chord length  $c$  ( $Re=3.4 \times 10^5$ ).  
 281 The rotational speed of the wind turbine is 39.84 rad/s. distance from the main inlet boundary  
 282 to the leading edge of the blade is  $10 \times c$  and the distance from the leading edge to the main  
 283 outlet boundary is  $20 \times c$ .



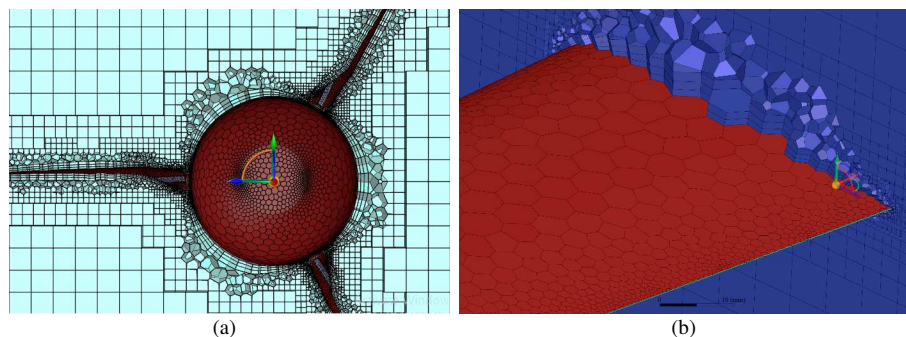
284

285 Figure 7: Computational domain used for the LES simulation. The length is indicated in terms of duct chord  
 286 length  $c$ .

287 According to Figure 8, the computational domain is discretized by about 6 million cells. The  
 288 fine mesh is used on the whole rotor surface and gradually becomes coarser as the distance  
 289 from the blades increases. Technique based on the previous results of  $k$ -epsilon turbulence  
 290 model have been used to evaluate the grid resolution in LES method. In this technique,  
 291 parameter  $f$ , has been calculated for the entire computing field by RANS model. The parameter  
 292  $f$  denotes the ratio of the integral turbulence length scale to the filter width. This can be  
 293 simplified and expressed as  $f = k^{3/2} / (\epsilon \times (\text{Cell Volume})^{1/3})$ , where  $k$  represents kinetic  
 294 energy and  $\epsilon$  signifies turbulent dissipation [36]. In most areas, this value is of the order of 5-  
 295 10, which indicates the good quality of the mesh. Therefore, the grid resolution meets the  
 296 requirements for the LES calculation.

This is the author's peer reviewed, accepted manuscript. However, the online version of record will be different from this version once it has been copyedited and typeset.

PLEASE CITE THIS ARTICLE AS DOI: 10.1063/1.50204050



297 Figure 8: Schematic view of the computational domain. (a) Front view of DWT and (b) Side view of the blade.

## 298 Results and Discussion

### 299 Validation

300 The validation method for this research was conducted with great attention to details. It  
 301 involved a rigorous comparison between the thrust force coefficient ( $C_T$ ), which is derived  
 302 from the pressure coefficient ( $C_p$ ) along the chord, and the reference data obtained from Ten  
 303 Hoopen's study described in reference [37]. The main objective was not to precisely reproduce  
 304 the  $C_p$  values at each location on the surface along the chord, but rather to guarantee that the  
 305 general pattern of  $C_p$  distribution closely corresponds to the reference, as illustrated in Figure  
 306 9. The key element of our validation process involved comparing the precise values of  $C_T$ , with  
 307 a specific emphasis on the correlation between the thrust ratio in our simulation and the  
 308 reference of [37].

309 It is important to note that Ten Hoopen's work lacks detailed information regarding the  
 310 manufacturing accuracy of the model and the precision of the measuring instruments. This  
 311 implies that achieving a precise match for local  $C_p$  values between the simulated results and  
 312 the reference data may not be possible. Hence, our validation focused on confirming the pattern  
 313 of behavior and the distribution curve of pressure.

314 In the present context, the validation of the simulation, which relies on the Donqi blade results  
 315 and is supplemented by the experimental findings of Ten Hoopen [37], demonstrates a  
 316 fundamental similarity in pressure distributions. However, there are slight variations observed  
 317 in the vicinity of the suction peak region, which may be attributed to assumptions made during  
 318 the simulation or inherent uncertainties in the experimental data. This validation verifies that  
 319 the aerodynamic characteristics of the ducted wind turbine (DWT) are accurately represented  
 320 and simulated, especially when examining how the pressure distributions react to different  
 321 wake propagation velocities ( $V_w$ ), which in turn affect the maximum absolute pressures on  
 322 various sides of the airfoil. Therefore, the duct thrust force coefficient ( $C_T$ ) has played a crucial  
 323 role in our work by calculating the grid resolution and assessing the aerodynamic changes in  
 324 the DWT models. This ensures that our technique closely matches the established experimental  
 325 standards. Table 3 presents a comparison of various grids against experimental and numerical

This is the author's peer reviewed, accepted manuscript. However, the online version of record will be different from this version once it has been copyedited and typeset.

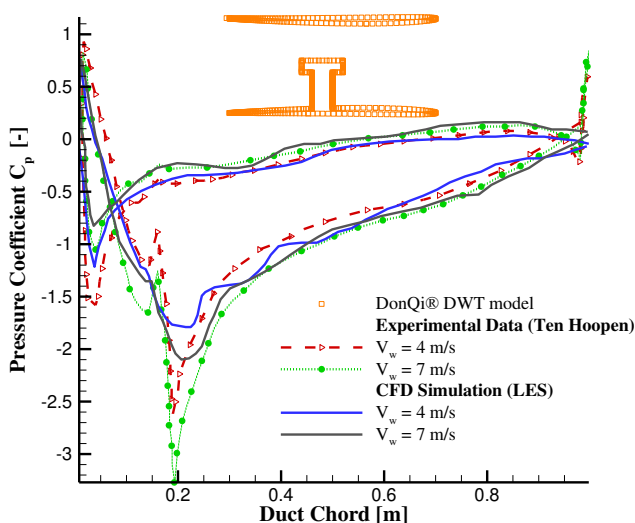
PLEASE CITE THIS ARTICLE AS DOI: 10.1063/1.50204050

326 results. The table indicates that the error for the 6 million grid was kept below 10%, meeting  
 327 the required accuracy standards. Therefore, the chosen grid number for this study was 6  
 328 million. The multi-section blade exhibited a 6.4 % increase in thrust force coefficient compared  
 329 to the conventional blade.

330

Table 3: Comparison of the thrust force coefficient.

	Experiment at Value [37]	2.7 million numerical value (Benchmark)	LES Error (%)	4.3 million numerical value (Benchmark)	LES Error (%)	6 million numerical value (Benchmark)	LES Error (%)	6 million numerical value (Multi- section)	Difference Value (percentage increase)
thrust force coefficient, $C_T$	0.689	0.811	17.7	0.773	12.2	0.735	6.7	0.782	6.4



331  
 332

Figure 9: Comparison between numerical and experimental solution of pressure distribution.

333 To validate the acoustic findings in our present study, we have conducted a comparative  
 334 analysis of the Power Spectral Density graph of the acoustic pressure, focusing on the blade  
 335 passing frequency, as illustrated in Figure 10. This evaluation was undertaken at the  
 336 microphone location set at 90 degrees for the DonQi® DWT model, as examined by Dighe et  
 337 al, [31]. It's evident that minimal deviations exist for blade passing frequencies below 2, with  
 338 more pronounced discrepancies emerging at higher frequencies. Overall distribution has  
 339 similar characteristic which the 2<sup>nd</sup> harmonic is less pronounced, and the 4<sup>th</sup> harmonic stronger.  
 340 Importantly, our LES approach not only captures these variations but also effectively  
 341 characterizes the transitional trends.

This is the author's peer reviewed, accepted manuscript. However, the online version of record will be different from this version once it has been copyedited and typeset.

PLEASE CITE THIS ARTICLE AS DOI: 10.1063/1.5204050

342  
343

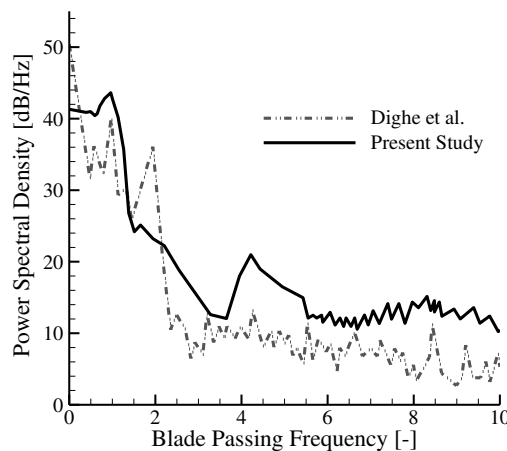
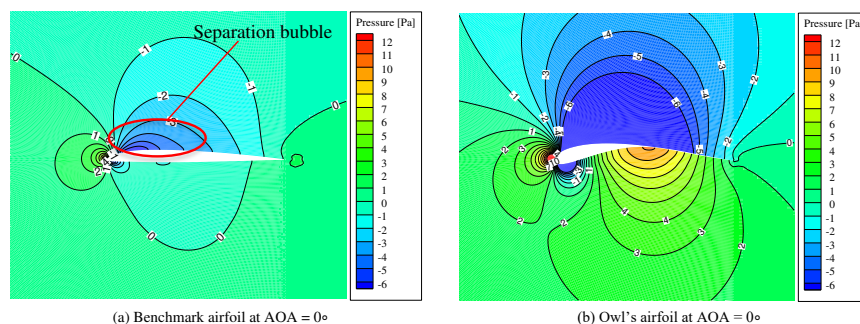


Figure 10: Validating Acoustic Results.

344 **Aerodynamics results**

345 This section focuses on the analysis of the characteristic of the owl airfoil compared to a  
346 conventional airfoil in a 2D context used for wind turbine. The evaluation is carried out by  
347 analyzing the aerodynamic properties of both types of airfoils, and the results are discussed in  
348 this section.

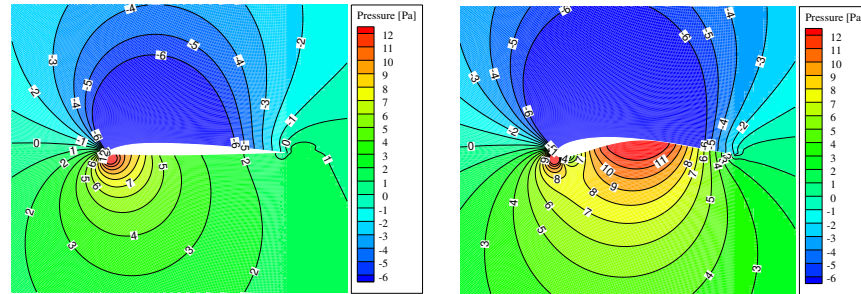
349 Figure 11 illustrate the pressure contour for the owl and benchmark airfoils at angles of attack  
350 of 0 and 6 degrees. The unique shape of the owl airfoil, characterized by a thicker leading edge,  
351 higher curvature, and thinner trailing edge, generates a separation bubble. More pronounced in  
352 the owl airfoil compared to a standard reference, leading to a more significant pressure  
353 difference and, in turn, increased lift (as depicted in Figure 12).



This is the author's peer reviewed, accepted manuscript. However, the online version of record will be different from this version once it has been copyedited and typeset.

PLEASE CITE THIS ARTICLE AS DOI: 10.1063/1.50204050

354



(c) Benchmark airfoil at AOA = 6° (d) Owl's airfoil at AOA = 6°  
Figure 11: The pressure contour at different angles of attack.

355  
356

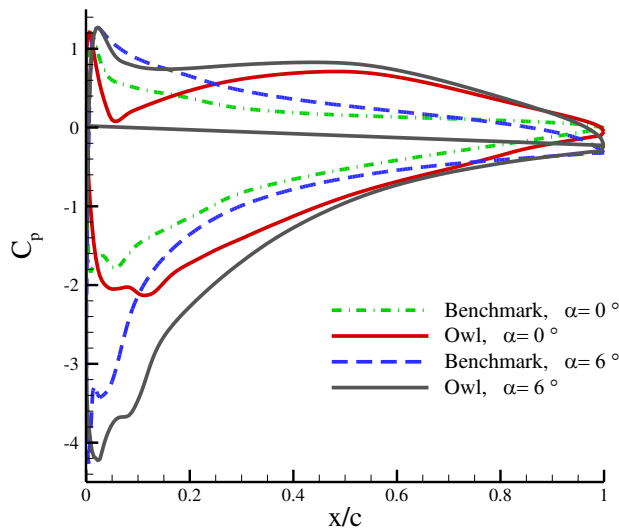
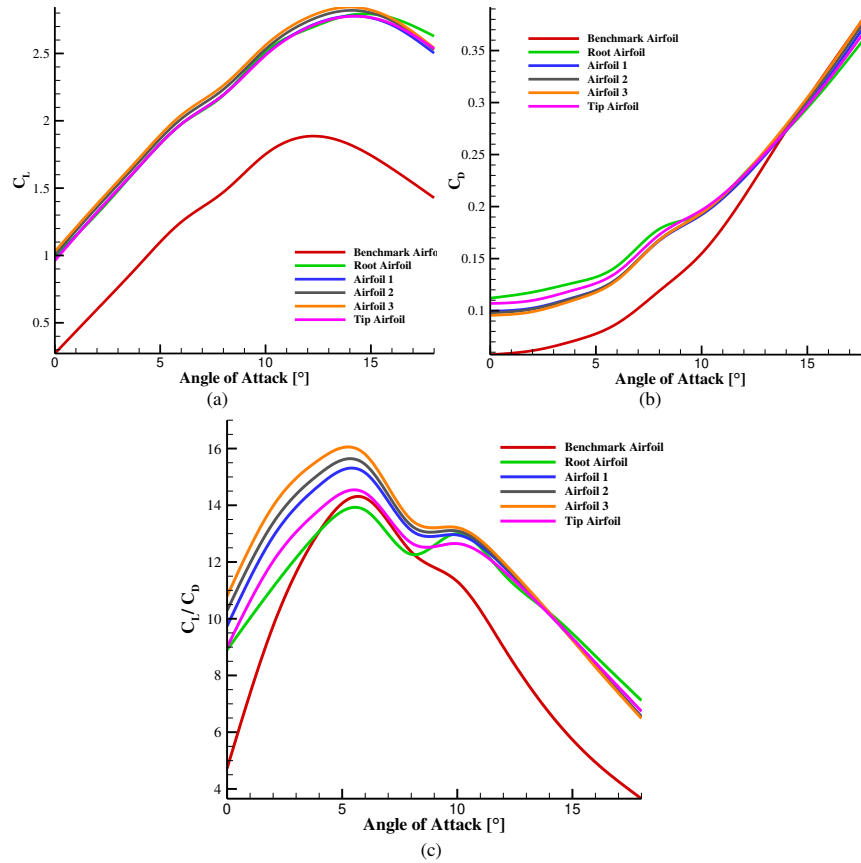


Figure 12: Cp comparison between Owl and benchmark airfoils for AOA= 0° and AOA= 6°.

357 In the owl airfoil, the blade's maximum camber, maximum thickness, and their respective  
 358 positions are altered, enhanced lift performance, increasing the maximum lift coefficient from  
 359 1.8 to 2.8 and raising the stall angle of attack from 12° to 14° (as shown in Figure 13a). While  
 360 the drag coefficient is higher for low attack angles in the owl airfoil, resulting in increased  
 361 drag, this is a necessary tradeoff for generating more lift (as shown in Figure 13b). However,  
 362 as shown in Figure 13c, the owl airfoil consistently outperforms the conventional airfoil in  
 363 terms of lift to drag ratio all angles of attack. There is a noticeable improvement in the lift-to-  
 364 drag ratio when the angle of attack reaches 5 degrees. Between angles of 8 to 10 degrees, the  
 365 aerodynamic performance remains relatively stable. However, beyond this range, in all  
 366 sections, there appears to be a decline in performance, possibly attributed to an increase in drag.

This is the author's peer reviewed, accepted manuscript. However, the online version of record will be different from this version once it has been copyedited and typeset.

PLEASE CITE THIS ARTICLE AS DOI: 10.1063/1.50204050



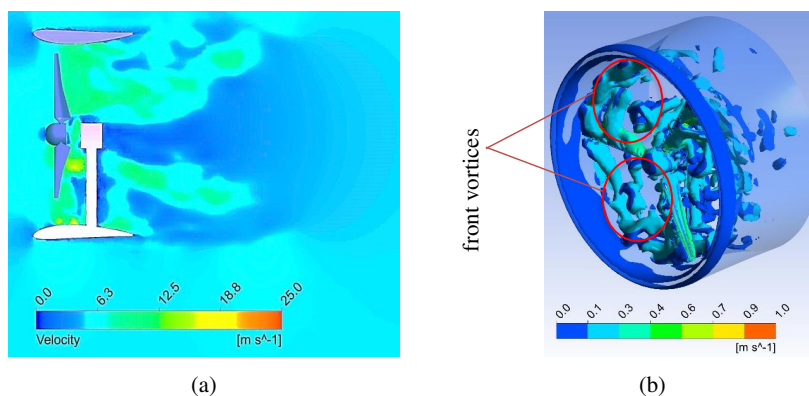
367 Figure 13: (a) Lift coefficients, (b) Drag coefficients and (c) Lift-to-drag ratio ( $C_l/C_d$ ) curves of the airfoils at  
 368 different AOA.

369 This section explores and presents the aerodynamic features of the turbine after the integration  
 370 of the owl airfoil. The implementation of the owl airfoil on the turbine is carried out, and the  
 371 resultant aerodynamic properties are studied and analyzed.

372 To better illustrate the changes in the flow field and interactions between the turbine and the  
 373 boundary layer as a result of the inlet flow, a 2D section of the flow velocity is shown in the  
 374 XY plane in Figure 14a. As can be seen, there are areas of low speed around the duct and  
 375 turbine holder. At the same time, there are also high-speed areas at the ends of the blades and  
 376 downstream (in the wake) which is 25 m/s. This indicates that the duct acts as a diffuser and  
 377 increases the speed of the incoming air.

378 For Case 2, the instantaneous flow fields around the ducted wind turbine are shown using the  
 379 Q criterion in Figure 14b. The figure illustrates the formation of vortices on the inner wall of

380 the duct. Due to the increase in camber and changes in the thickness of the airfoil as the flow  
 381 moves along the inner wall of the duct, the speed of the flow increases. The front vortices  
 382 originate from the starting point of the inner side of the duct and adopt a helical shape as they  
 383 get closer to the turbine. Consequently, this leads to an increase in turbulence structures and an  
 384 increase in Turbulence Intensity (TI), which ultimately breaks up the larger front vortices into  
 385 smaller ones. It also shows that the LES turbulence model predicts the turbulence fluctuations  
 386 around a DWT well and provides a clearer picture of the complex flows around the turbine.



387 Figure 14: (a) Velocity contour, (b) Q criterion.

388 In the context of a wind turbine, the conversion of mechanical energy into electrical energy  
 389 hinges on the performance of the aerodynamic system, quantified as the power coefficient  
 390 ( $C_{PWR}$ ). In parallel, an essential factor in the design of turbine blades is the Tip Speed Ratio  
 391 (TSR), representing the ratio between the linear speed of the blade tip and the wind speed.  
 392 Consequently, this section delves into the variations in the power coefficient concerning TSR  
 393 for both benchmark and multi-section blades. As illustrated in Figure 15,  $C_{PWR}$  exhibits a non-  
 394 linear relationship with TSR, with the maximum  $C_{PWR}$  value occurring at  $TSR = 8$  in both  
 395 cases. This maximum value signifies the peak efficiency of the DWT. Thus, the selection of  
 396 the optimal TSR value is of paramount importance. Furthermore, as depicted in the figure 15,  
 397 for TSR values below 5, there is negligible discrepancy in  $C_{PWR}$  between the two blade types,  
 398 with their performance differing by less than 10%. However, as TSR values increase, the  $C_{PWR}$   
 399 parameter demonstrates a significant rise, underscoring the benefit of employing multi-section  
 400 blades.

This is the author's peer reviewed, accepted manuscript. However, the online version of record will be different from this version once it has been copyedited and typeset.

PLEASE CITE THIS ARTICLE AS DOI: 10.1063/1.5204050

401  
402  
403

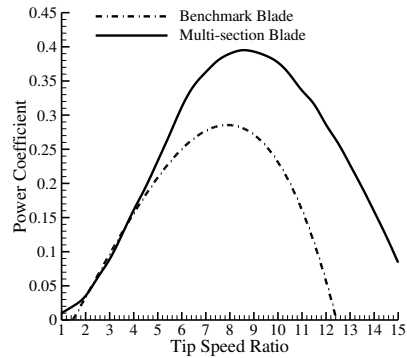
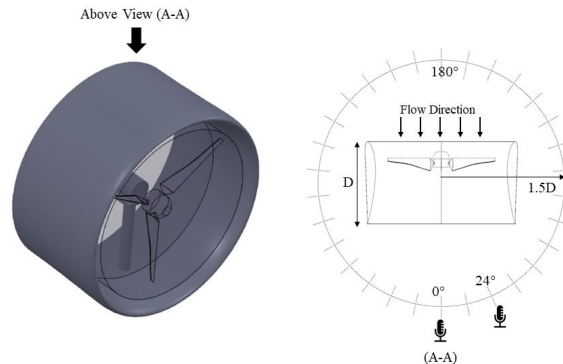


Figure 15: Variation in Power Coefficients for Benchmark and Multi-Section Blades across Various Tip Speed Ratio.

404 **Aeroacoustics results**

405 To investigate the sound around the turbine, according to Figure 16, thirty receivers are being  
406 used in the current study. The receivers are positioned at a distance of 1.5 times the chord  
407 length of the Duct airfoil. Receivers are spaced 12 degrees apart.



408  
409

Figure 16: Receivers position.

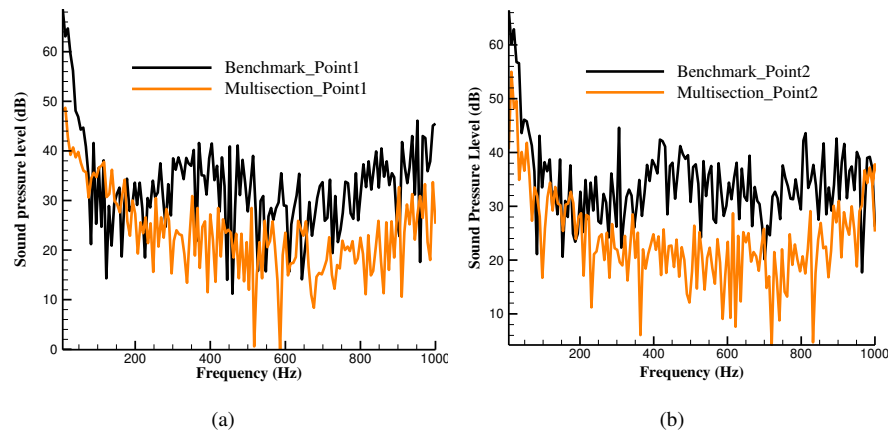
410 Based on the receiver position curve, two specific points are analyzed in this study, point 1 at  
411 0 degrees and point 2 at 24 degrees. Figure 17 displays sound pressure level graphs for both  
412 points, showing the frequency response for two cases. By implementing owl wing airfoils,  
413 noise generated by free stream turbulence and trailing edge noise is reduced. Notably, this  
414 improvement has the most significant impact on higher frequencies. The multi-section results  
415 suggest that owl-inspired airfoils have proven effective in mitigating noise.

416 According to the polar curve of Overall Sound Pressure Level (OASPL), as shown in Figure  
417 18 based on the position of the receivers, it can be seen that the use of airfoils of owl-inspired  
418 reduces the sound by an average of 6-8 decibels at 60 to -60 degrees (which represents the flow

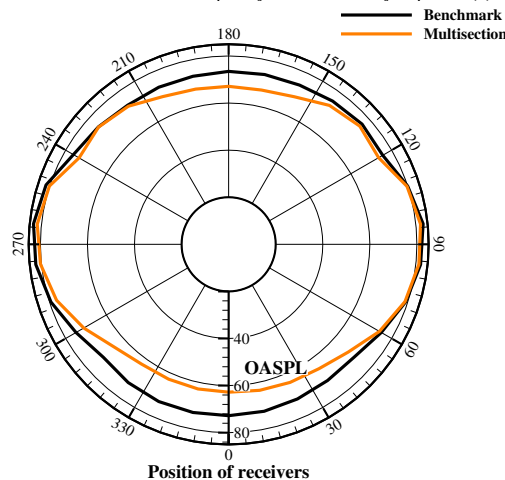
This is the author's peer reviewed, accepted manuscript. However, the online version of record will be different from this version once it has been copyedited and typeset.

PLEASE CITE THIS ARTICLE AS DOI: 10.1063/1.5204050

419 exit area from the duct). As can be seen, in some positions, including 90 and 270 degrees, there  
 420 is no change in the OASPL curve for owl-shaped wing (multi-section blade). It does not reduce  
 421 sound in the radial direction. As a result, to reduce sound, it is recommended to make changes  
 422 such as using perforated plates in the structure of the duct and its surfaces, as well as adding  
 423 sound-absorbing materials inside.



424 Figure 17: Comparison between SPL vs Frequency of 2 cases study at point1 (a) and point2 (b).



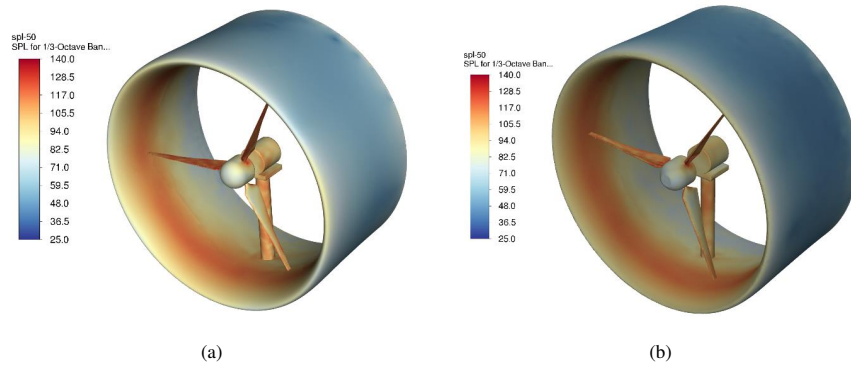
425  
 426 Figure 18: Comparison between SPL of 2 cases study around the ducted.

427 As can be seen in Figure 19a, the highest sound pressure level occurs on the inner surface of  
 428 the duct which the lowest level is on the outer surfaces of the duct. The highest SPL value on  
 429 the inner surface of the duct is typically associated with the airfoil's thickest portion located at  
 430 the leading edge. As a result, the use of a duct as a diffuser cover significantly reduces the  
 431 sound and act as a barrier, as well as protect the surrounding environment from damage. Based

This is the author's peer reviewed, accepted manuscript. However, the online version of record will be different from this version once it has been copyedited and typeset.

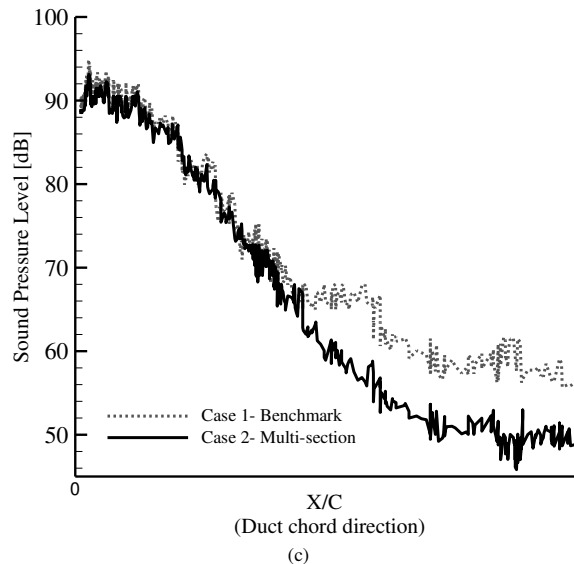
PLEASE CITE THIS ARTICLE AS DOI: 10.1063/1.5204050

432 on the contour presented in figure 19b, it appears that altering the blade foils did not result in  
 433 any detrimental impact on the level of noise produced at the tip of the turbine duct. Also, figures  
 434 19 illustrates how the surface under the airfoil, which is the suction area, has a more significant  
 435 effect on noise production. An explanation for this can be found in the change in the camber  
 436 line and the changes in the thickness of the airfoil. Therefore, it leads to an increase in  
 437 turbulence structures and pressure fluctuations, resulting in more sound being produced on the  
 438 lower surface of the airfoil. With comparing Figures 19a and 19b, it becomes apparent that the  
 439 SPL value has decreased both downstream and on the inner surface of the duct. Further analysis  
 440 can be conducted by referring to Figure 19c, which illustrates sound pressure levels specifically  
 441 along the inner surface of the duct. In this segment, a section is formed on the interior of the  
 442 duct. It is worth noting that modifications made to the turbine blade have a noticeable effect on  
 443 the noise generated downstream, leading to a reduction in noise at the trailing edge of the inner  
 444 duct. This noise reduction is approximately equal to 10 dB in all positions after the turbine  
 445 tower. Intriguingly, the use of multi-section blades does not impact the noise levels in front of  
 446 the rotor.  
 447



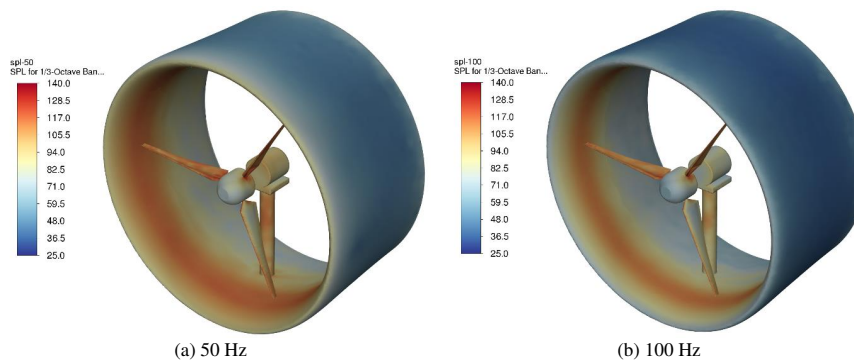
This is the author's peer reviewed, accepted manuscript. However, the online version of record will be different from this version once it has been copyedited and typeset.

PLEASE CITE THIS ARTICLE AS DOI: 10.1063/1.5204050



448 Figure 19: Noise level contour for frequency 50 Hz for cases number 1 (a) and 2 (b) and (c) Comparative  
 449 Analysis of Sound Pressure Levels along the Inner Duct Surface between Cases 1 and 2.

450 Upon analyzing the frequencies ranging from 50 Hz to 500 Hz in case number 2 as shown in  
 451 Figure 20, it becomes apparent that noise levels decrease as the frequency increases. The  
 452 maximum noise production within the duct occurs in the regions near the leading edge to the  
 453 tower, with the highest levels of noise generated in the corresponding areas of the blade tips.  
 454 Also, this figure indicates that the most effective place to reduce noise is this area, which is the  
 455 logical point to consider the perforated plate (punch) along with the absorber at the position of  
 456 the inner junction to the turbine tower to the duct.



This is the author's peer reviewed, accepted manuscript. However, the online version of record will be different from this version once it has been copyedited and typeset.

PLEASE CITE THIS ARTICLE AS DOI: 10.1063/1.5204050

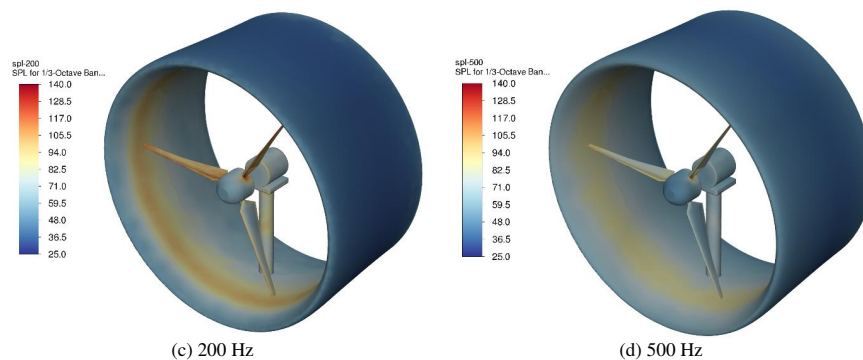


Figure 20: Noise level contour for frequencies 50 Hz to 500 Hz for case number 2.

457

### 458 **Conclusions**

459 In this comprehensive study, we have employed advanced Large Eddy Simulation (LES)  
 460 turbulence modeling and Ffowcs Williams-Hawkings (FW-H) acoustic analogy to  
 461 meticulously analyze the aeroacoustic and aerodynamic properties of ducted wind turbine  
 462 blades. These blades are innovatively designed, drawing inspiration from the silent flight  
 463 mechanism of owl wings. Our primary aim was to address the critical challenge of reducing  
 464 aerodynamic noise, particularly the noise generated by inflow turbulence and trailing edges,  
 465 while concurrently ensuring that the aerodynamic performance remains uncompromised.

466 The investigation revealed that the incorporation of bio-inspired airfoil sections, meticulously  
 467 derived from owl wings through 3D scanning techniques, significantly influences the noise  
 468 reduction and aerodynamic efficiency of wind turbines. Specifically, the application of these  
 469 uniquely designed airfoils resulted in a notable reduction of aerodynamic noise by  
 470 approximately 8 decibels, which translates to an improvement of about 12% when compared  
 471 to conventional designs. This achievement underscores the potential of bio-inspired  
 472 modifications in enhancing the environmental compatibility of wind turbines, particularly in  
 473 urban settings where noise pollution is a significant concern.

474 Moreover, our results demonstrated a 6.4% increase in the thrust force coefficient for the multi-  
 475 section blade compared to the conventional blade design. The power coefficient analysis  
 476 further revealed that the maximum power coefficient occurred at a Tip Speed Ratio (TSR) of  
 477 8 for both the benchmark and multi-section blades, emphasizing the optimized aerodynamic  
 478 efficiency achieved through the bio-inspired design.

479 Furthermore, our study delved into the aeroacoustic performance, where the findings indicated  
 480 a substantial noise reduction in specific areas around the duct, especially downstream and on  
 481 the inner surface. These results suggest that the strategic implementation of owl-inspired airfoil  
 482 profiles not only benefits the noise profile but also contributes to the overall aerodynamic  
 483 efficiency of the turbine. However, it's worth noting that the radial sound suppression remained  
 484 unaffected, suggesting additional avenues for enhancing the aeroacoustic performance,  
 485 possibly through further structural modifications or the integration of sound-absorbing  
 486 materials.

487 In conclusion, this research not only contributes valuable insights into the aeroacoustic and  
 488 aerodynamic optimization of wind turbines but also highlights the potential of bio-inspired  
 489 designs in the field of renewable energy. The significant reduction in noise levels, coupled with  
 490 the maintenance of aerodynamic performance, presents a compelling case for the adoption of

491 such innovative design strategies in future wind turbine development, particularly in noise-  
 492 sensitive environments. Our findings lay a solid foundation for future studies and the practical  
 493 application of bio-inspired designs in enhancing the sustainability and community acceptance  
 494 of wind energy solutions.

#### 495 **Data Availability**

496 The data used to support the findings of this study are available from the corresponding author  
 497 upon request.

#### 498 **Conflicts of Interest**

499 The authors declare that there is no conflict of interest regarding the publication of this paper.

#### 500 **Funding Statement**

501 The authors have no relevant financial or non-financial interests to disclose.

#### 502 **Acknowledgments**

503 Our research would not have been possible without the support of Iran Wildlife and Nature  
 504 Museum - Dar Abad and Huber 3D scan engineering group, who provided us with a great deal  
 505 of assistance.

#### 506 **References**

- 507 [1] A.H. Butt, B. Akbar, J. Aslam, N. Akram, M.E.M. Soudagar, F.P.G. Márquez, M.Y. Younis, E. Uddin,  
 508 "Development of a linear acoustic array for aero-acoustic quantification of camber-bladed vertical axis  
 509 wind turbine," *Sensors (Switzerland)*, vol. 20, pp. 1-17, 2020.
- 510 [2] M. Ilie, J.W. McAfee, "Aerodynamics and design of vertical-axis wind turbine; numerical studies using  
 511 les and iddes," in *AIAA AVIATION 2020 FORUM*, 2020, pp. 1-9.
- 512 [3] T. Fukano, C.-M. Jang, "Tip clearance noise of axial flow fans operating at design and off-design  
 513 condition," *Journal of sound and vibration*, vol. 275, pp. 1027-1050, 2004.
- 514 [4] H. Weger, M. Weger, M. Klaas, W. Schröder, "Features of owl wings that promote silent flight,"  
 515 *Interface Focus*, vol. 7, 2017.
- 516 [5] R. Graham, "The silent flight of owls," *The Aeronautical Journal*, vol. 38, pp. 837-843, 1934.
- 517 [6] E. Mascha, "Über die schwungfedern," *Zeitschrift für wissenschaftliche Zoologie*, vol. 77, pp. 606-651,  
 518 1904.
- 519 [7] L. Wang, X. Liu, D. Li, "Noise reduction mechanism of airfoils with leading-edge serrations and surface  
 520 ridges inspired by owl wings," *Physics of Fluids*, vol. 33, 2021.
- 521 [8] R. Hayden, "Reduction of noise from airfoils and propulsive lift systems using variable impedance  
 522 systems," in *3rd AIAA Aeroacoustics Conf.*, Palo Alto, CA, USA, 1976.
- 523 [9] P. Chaitanya, P. Joseph, S. Narayanan, C. Vanderwel, J. Turner, J.-W. Kim, B. Ganapathisubramani,  
 524 "Performance and mechanism of sinusoidal leading edge serrations for the reduction of turbulence-  
 525 aerofoil interaction noise," *Journal of Fluid Mechanics*, vol. 818, pp. 435-464, 2017.
- 526 [10] B.Y. Zhou, S.R. Koh, N.R. Gauger, M. Meinke, W. Schöder, "A discrete adjoint framework for trailing-  
 527 edge noise minimization via porous material," *Computers & Fluids*, vol. 172, pp. 97-108, 2018.
- 528 [11] C. Pimenta, W.R. Wolf, A.V. Cavaliere, "A fast numerical framework to compute acoustic scattering by  
 529 poroelastic plates of arbitrary geometry," *Journal of Computational Physics*, vol. 373, pp. 763-783, 2018.
- 530 [12] J.M. Turner, J.W. Kim, "Aeroacoustic source mechanisms of a wavy leading edge undergoing vortical  
 531 disturbances," *Journal of Fluid mechanics*, vol. 811, pp. 582-611, 2017.
- 532 [13] E. Sarradj, C. Fritzsche, T. Geyer, "Silent owl flight: Bird flyover noise measurements," *AIAA journal*,  
 533 vol. 49, pp. 769-779, 2011.
- 534 [14] K. Lee, Y. Kozato, S. Kikuchi, S. Imao, "Numerical simulation of flow control around a rectangular  
 535 cylinder by dielectric barrier discharge plasma actuators," *Physics of Fluids*, vol. 34, 2022.

This is the author's peer reviewed, accepted manuscript. However, the online version of record will be different from this version once it has been copyedited and typeset.

PLEASE CITE THIS ARTICLE AS DOI: 10.1063/1.50204050

- 536 [15] E. Fatahian, F. Ismail, M.H.H. Ishak, W.S. Chang, "Aerodynamic performance improvement of savonius  
537 wind turbine through a passive flow control method using grooved surfaces on a deflector," *Ocean*  
538 *Engineering*, vol. 284, p. 115282, 2023.
- 539 [16] F. Eydi, A. Mojra, R. Abdi, "Comparative analysis of the flow control over a circular cylinder with  
540 detached flexible and rigid splitter plates," *Physics of Fluids*, vol. 34, 2022.
- 541 [17] W. Song, Z. Mu, Y. Wang, Z. Zhang, S. Zhang, Z. Wang, B. Li, J. Zhang, S. Niu, Z. Han, "Comparative  
542 investigation on improved aerodynamic and acoustic performance of abnormal rotors by bionic edge  
543 design and rational material selection," *Polymers*, vol. 14, p. 2552, 2022.
- 544 [18] T. Liu, K. Kuykendoll, R. Rhew, S. Jones, "Avian wing geometry and kinematics," *AIAA journal*, vol.  
545 44, pp. 954-963, 2006.
- 546 [19] S. Klačn, T. Bachmann, M. Klaas, H. Wagner, W. Schröder, "Experimental analysis of the flow field over  
547 a novel owl based airfoil," *Animal Locomotion*, pp. 413-427, 2010.
- 548 [20] T. Bachmann, G. Mühlenbruch, H. Wagner, "The barn owl wing: An inspiration for silent flight in the  
549 aviation industry?," in *Bioinspiration, Biomimetics, and Bioreplication*, 2011, pp. 142-155.
- 550 [21] T. Geyer, E. Sarraj, C. Fritzsche, "Silent owl flight: Acoustic wind tunnel measurements on prepared  
551 wings," in *18th AIAA/CEAS Aeroacoustics Conference (33rd AIAA Aeroacoustics Conference)*, 2012,  
552 p. 2230.
- 553 [22] K. Kondo, H. Aono, T. Nonomura, M. Anyoji, A. Oyama, T. Liu, K. Fujii, M. Yamamoto, "Analysis of  
554 owl-like airfoil aerodynamics at low reynolds number flow," *Transactions of the Japan Society for*  
555 *Aeronautical and Space Sciences, Aerospace Technology Japan*, vol. 12, pp. Tk\_35-Tk\_40, 2014.
- 556 [23] W. Tian, Z. Yang, Q. Zhang, J. Wang, M. Li, Y. Ma, Q. Cong, "Bionic design of wind turbine blade  
557 based on long-eared owl's airfoil," *Applied Bionics and Biomechanics*, vol. 2017, 2017.
- 558 [24] M. Anyoji, S. Wakui, D. Hamada, H. Aono, "Experimental study of owl-like airfoil aerodynamics at low  
559 reynolds numbers," *Journal of Flow Control, Measurement & Visualization*, vol. 6, p. 185, 2018.
- 560 [25] F. Moslem, M. Masdari, K. Fedir, B. Moslem, "Experimental investigation into the aerodynamic and  
561 aeroacoustic performance of bioinspired small-scale propeller planforms," *Proceedings of the Institution*  
562 *of Mechanical Engineers, Part G: Journal of Aerospace Engineering*, vol. 237, pp. 75-90, 2023.
- 563 [26] H. Aono, K. Kondo, T. Nonomura, M. Anyoji, A. Oyama, K. Fujii, M. Yamamoto, "Aerodynamics of  
564 owl-like wing model at low reynolds numbers," *Transactions of the Japan Society for Aeronautical and*  
565 *Space Sciences*, vol. 63, pp. 8-17, 2020.
- 566 [27] M. Muthuramalingam, E. Talboys, H. Wagner, C. Bruecker, "Flow turning effect and laminar control by  
567 the 3d curvature of leading edge serrations from owl wing," *Bioinspiration & Biomimetics*, vol. 16, p.  
568 026010, 2020.
- 569 [28] N. Ricks, P. Tsirikoglou, F. Contino, G. Ghorbaniasl, "A cfd-based methodology for aerodynamic-  
570 aeroacoustic shape optimization of airfoils," in *AIAA Scitech 2020 Forum*, 2020, p. 1729.
- 571 [29] H. Gruschka, I. Borchers, J. Coble, "Aerodynamic noise produced by a gliding owl," *Nature*, vol. 233,  
572 pp. 409-411, 1971.
- 573 [30] T. Wolf, R. Konrath, "Avian wing geometry and kinematics of a free-flying barn owl in flapping flight,"  
574 *Experiments in Fluids*, vol. 56, pp. 1-18, 2015.
- 575 [31] V.V. Dighe, F. Avallone, G. van Bussel, "Effects of yawed inflow on the aerodynamic and aeroacoustic  
576 performance of ducted wind turbines," *Journal of Wind Engineering and Industrial Aerodynamics*, vol.  
577 201, 2020.
- 578 [32] K. Güzey, U.E. Aylı, E. Kocak, S. Aradag, "Investigation of aerodynamic and aeroacoustic behavior of  
579 bio-inspired airfoils with numerical and experimental methods," *Proceedings of the Institution of*  
580 *Mechanical Engineers, Part C: Journal of Mechanical Engineering Science*, p. 09544062231185495,  
581 2023.
- 582 [33] F. Eydi, A. Mojra, "A numerical study on the benefits of passive-arc plates on drag and noise reductions  
583 of a cylinder in turbulent flow," *Physics of Fluids*, vol. 35, 2023.
- 584 [34] Y. Wang, T. Mikkola, S. Hirdaris, "A fast and storage-saving method for direct volumetric integration  
585 of fwh acoustic analogy," *Ocean Engineering*, vol. 261, p. 112087, 2022.
- 586 [35] D. Romik, I. Czajka, "Numerical investigation of the sensitivity of the acoustic power level to changes  
587 in selected design parameters of an axial fan," *Energies*, vol. 15, p. 1357, 2022.
- 588 [36] S. Gant, "Practical quality measures for large-eddy simulation," in *Direct and Large-Eddy Simulation*  
589 *VII: Proceedings of the Seventh International ERCOFTAC Workshop on Direct and Large-Eddy*  
590 *Simulation*, held at the University of Trieste, September 8-10, 2008, 2010, pp. 217-222.
- 591 [37] T. Hoopen, "An experimental and computational investigation of a diffuser augmented wind turbine:  
592 With an application of vortex generators on the diffuser trailing edge," Ph.D. thesis, Delft University of  
593 Technology, Delft, The Netherlands, 2009.
- 594